# Technical University of Denmark

**DTU**

# Highly coherent mid-IR supercontinuum by self-defocusing solitons in lithium niobate waveguides with all-normal dispersion

**Guo, Hairun; Zhou, Binbin; Zeng, Xianglong; Bache, Morten**

[Link back to DTU Orbit](Link back to DTU Orbit)

**DTU Library**
Technical Information Center of Denmark

# Highly coherent mid-IR supercontinuum by self-defocusing solitons in lithium niobate waveguides with all-normal dispersion

**Hairun Guo,**[1] **Binbin Zhou,**[1] **Xianglong Zeng,**[2,3] **and Morten Bache**[1,*]

[1]*DTU-Fotonik, Department of Photonics Engineering Technical University of Denmark, DK-2800, Kgs. Lyngby, Denmark*
[2]*Key Laboratory of Special Fiber Optics and Optical Access Networks, Shanghai University, Shanghai 200072, China*
[3]*zenglong@shu.edu.cn*
[*]*moba@fotonik.dtu.dk*

**Abstract:** We numerically investigate self-defocusing solitons in a lithium niobate (LN) waveguide designed to have a large refractive index (RI) change. The waveguide evokes strong waveguide dispersion and all-normal dispersion is found in the entire guiding band spanning the near-IR and the beginning of the mid-IR. Meanwhile, a self-defocusing nonlinearity is invoked by the cascaded (phase-mismatched) second-harmonic generation under a quasi-phase-matching pitch. Combining this with the all-normal dispersion, mid-IR solitons can form and the waveguide presents the first all-nonlinear and solitonic device where no linear dispersion (i.e. non-solitonic) regimes exist within the guiding band. Soliton compressions at 2 $\mu$m and 3 $\mu$m are investigated, with nano-joule single cycle pulse formations and highly coherent octave-spanning supercontinuum generations. With an alternative design on the waveguide dispersion, the soliton spectral tunneling effect is also investigated, with which few-cycle pico-joule pulses at 2 $\mu$m are formed by a near-IR pump.

© 2014 Optical Society of America

**OCIS codes:** (230.7370) Waveguides; (320.5520) Pulse compression; (320.6629) Supercontinuum generation; (320.7110) Ultrafast nonlinear optics.

## References and links

1. P. A. Franken, A. E. Hill, C. W. Peters, and G. Weinreich, "Generation of optical harmonics," Phys. Rev. Lett. **7**, 118–119 (1961).
2. S. Ashihara, J. Nishina, T. Shimura, and K. Kuroda, "Soliton compression of femtosecond pulses in quadratic media," J. Opt. Soc. Am. B **19**, 2505–2510 (2002).
3. J. Moses and F. W. Wise, "Soliton compression in quadratic media: high-energy few-cycle pulses with a frequency-doubling crystal," Opt. Lett. **31**, 1881–1883 (2006).
4. B. B. Zhou, A. Chong, F. W. Wise, and M. Bache, "Ultrafast and octave-spanning optical nonlinearities from strongly phase-mismatched quadratic interactions," Phys. Rev. Lett. **109**, 043902 (2012).
5. R. DeSalvo, H. Vanherzeele, D. J. Hagan, M. Sheik-Bahae, G. Stegeman, and E. W. V. Stryland, "Self-focusing and self-defocusing by cascaded second-order effects in KTP," Opt. Lett. **17**, 28–30 (1992).
6. M. L. Sundheimer, J. D. Bierlein, C. Bosshard, E. W. V. Stryland, and G. I. Stegeman, "Large nonlinear phase modulation in quasi-phase-matched KTP waveguides as a result of cascaded second-order processes," Opt. Lett. **18**, 1397–1399 (1993).

7. G. I. Stegeman, M. Sheik-Bahae, E. V. Stryland, and G. Assanto, "Large nonlinear phase shifts in second-order nonlinear-optical processes," Opt. Lett. **18**, 13–15 (1993).
8. C. R. Menyuk, R. Schiek, and L. Torner, "Solitary waves due to $\chi^{(2)}$: $\chi^{(2)}$ cascading," J. Opt. Soc. Am. B **11**, 2434–2443 (1994).
9. C. Langrock, S. Kumar, J. McGeehan, A. Willner, and M. Fejer, "All-optical signal processing using $\chi^{(2)}$ nonlinearities in guided-wave devices," J. Lightwave Technol. **24**, 2579–2592 (2006).
10. R. Schiek, H. Seibert, W. Sohler, M. L. Sundheimer, D. Y. Kim, Y. Baek, and G. I. Stegeman, "Direct measurement of cascaded nonlinearity in lithium niobate channel waveguides," Opt. Lett. **19**, 1949–1951 (1994).
11. R. Schiek, Y. Baek, and G. I. Stegeman, "Second-harmonic generation and cascaded nonlinearity in titanium-indiffused lithium niobate channel waveguides," J. Opt. Soc. Am. B **15**, 2255–2268 (1998).
12. M. L. Bortz and M. M. Fejer, "Annealed proton-exchanged LiNbO$_3$ waveguides," Opt. Lett. **16**, 1844–1846 (1991).
13. K. Gallo, J. Prawiharjo, N. Broderick, and D. Richardson, "Proton-exchanged LiNbO$_3$ waveguides for photonic applications," in *Proceedings of 6th International Conference on Transparent Optical Networks* (2004), **1**, 277–281.
14. H. Guo, X. Zeng, B. Zhou, and M. Bache, "Few-cycle solitons and supercontinuum generation with cascaded quadratic nonlinearities in unpoled lithium niobate ridge waveguides," Opt. Lett. **39**, 1105–1108 (2014).
15. C. R. Phillips, C. Langrock, J. S. Pelc, M. M. Fejer, J. Jiang, M. E. Fermann, and I. Hartl, "Supercontinuum generation in quasi-phase-matched LiNbO$_3$ waveguide pumped by a Tm-doped fiber laser system," Opt. Lett. **36**, 3912–3914 (2011).
16. C. R. Phillips, C. Langrock, J. S. Pelc, M. M. Fejer, I. Hartl, and M. E. Fermann, "Supercontinuum generation in quasi-phasematched waveguides," Opt. Express **19**, 18754–18773 (2011).
17. C. Langrock, M. M. Fejer, I. Hartl, and M. E. Fermann, "Generation of octave-spanning spectra inside reverse-proton-exchanged periodically poled lithium niobate waveguides," Opt. Lett. **32**, 2478–2480 (2007).
18. M. Bache, H. Guo, and B. Zhou, "Generating mid-IR octave-spanning supercontinua and few-cycle pulses with solitons in phase-mismatched quadratic nonlinear crystals," Opt. Mater. Express **3**, 1647–1657 (2013).
19. D. V. Skryabin and A. V. Gorbach, "*Colloquium*: Looking at a soliton through the prism of optical supercontinuum," Rev. Mod. Phys. **82**, 1287–1299 (2010).
20. O. Tadanaga, T. Yanagawa, Y. Nishida, H. Miyazawa, K. Magari, M. Asobe, and H. Suzuki, "Efficient 3-$\mu$m difference frequency generation using direct-bonded quasi-phase-matched LiNbO$_3$ ridge waveguides," Appl. Phys. Lett. **88**, 061101 (2006).
21. P. Rabiei, J. Ma, S. Khan, J. Chiles, and S. Fathpour, "Heterogeneous lithium niobate photonics on silicon substrates," Opt. Express **21**, 25573–25581 (2013).
22. M. Bass, C. DeCusatis, J. Enoch, V. Lakshminarayanan, G. Li, C. MacDonald, V. Mahajan, and E. Van Stryland, *Handbook of Optics*, Vol. IV of Optical Properties of Materials, Nonlinear Optics, Quantum Optics (set), 3rd ed. (McGraw-Hill Education, 2009), Chap. 2.
23. A. M. Heidt, "Pulse preserving flat-top supercontinuum generation in all-normal dispersion photonic crystal fibers," J. Opt. Soc. Am. B **27**, 550–559 (2010).
24. H. Guo, X. Zeng, and M. Bache, "Generalized nonlinear Wwave equation in frequency domain," arXiv:1301.1473 (2013).
25. M. Bache, "Designing microstructured polymer optical fibers for cascaded quadratic soliton compression of femtosecond pulses," J. Opt. Soc. Am. B **26**, 460–470 (2009).
26. M. Bache, O. Bang, J. Moses, and F. W. Wise, "Nonlocal explanation of stationary and nonstationary regimes in cascaded soliton pulse compression," Opt. Lett. **32**, 2490–2492 (2007).
27. H. Guo, X. Zeng, B. Zhou, and M. Bache, "Nonlinear wave equation in frequency domain: accurate modeling of ultrafast interaction in anisotropic nonlinear media," J. Opt. Soc. Am. B **30**, 494–504 (2013).
28. M. Bache and R. Schiek, "Review of measurements of Kerr nonlinearities in lithium niobate: the role of the delayed Raman response," arXiv:1211.1721 (2012).
29. V. N. Serkin, T. L. Belyaeva, G. H. Corro, and M. A. Granados, "Stimulated raman self-scattering of femtosecond pulses. I. soliton and non-soliton regimes of coherent self-scattering," Quantum Electron. **33**, 325 (2003).
30. J. M. Dudley, G. Genty, and S. Coen, "Supercontinuum generation in photonic crystal fiber," Rev. Mod. Phys. **78**, 1135–1184 (2006).
31. V. Serkin, V. Vysloukh, and J. Taylor, "Soliton spectral tunnelling effect," Electron. Lett. **29**, 12–13 (1993).
32. M. Bache, O. Bang, B. B. Zhou, J. Moses, and F. W. Wise, "Optical cherenkov radiation by cascaded nonlinear interaction: an efficient source of few-cycle energetic near- to mid-IR pulses," Opt. Express **19**, 22557–22562 (2011).
33. N. Akhmediev and M. Karlsson, "Cherenkov radiation emitted by solitons in optical fibers," Phys. Rev. A **51**, 2602–2607 (1995).
34. D. V. Skryabin, F. Luan, J. C. Knight, and P. S. J. Russell, "Soliton self-frequency shift cancellation in photonic crystal fibers," Science **301**, 1705–1708 (2003).
35. H. Guo, S. Wang, X. Zeng, and M. Bache, "Understanding soliton spectral tunneling as a spectral coupling effect," IEEE Photon. Technol. Lett. **25**, 1928–1931 (2013).

36. M. Bache, O. Bang, B. B. Zhou, J. Moses, and F. W. Wise, "Optical Cherenkov radiation in ultrafast cascaded second-harmonic generation," Phys. Rev. A **82**, 063806 (2010).

## 1. Introduction

Quadratic nonlinear materials were used for the first nonlinear optics experiment known as the second harmonic generation (SHG) [1]. Besides frequency conversion achieved under phase-matching conditions, quadratic nonlinear crystals such as barium borate (BBO) and lithium niobate (LN) are attractive when operated far from phase matching for self-defocusing soliton compressions [2–4]. It is based on the cascaded (strongly phase-mismatched) quadratic non-linearity, such as SHG, which effectively acts like a cubic Kerr nonlinearity [5–8] that can be tuned in sign and magnitude through the phase-mismatch parameter. In particular a self-defocusing nonlinearity is of great interests as solitons can form with normal dispersion [2]. As the self-defocusing nonlinearity governs the pulse nonlinear dynamics there are no self-focusing problems, and therefore strong nonlinear interactions occur without any pulse energy limit, leading to the generation of ultra-high intensity and few-cycle soliton pulses.

LN cut for noncritical SHG, where the pump and its second harmonic (SH) have parallel polarizations, turns out to inherently produce an overall self-defocusing cascading nonlinearity over a wide wavelength span in the near- and mid-IR region. This was used for soliton self-compression and supercontinuum generation in a bulk LN crystal [4], but is equally promising to exploit cascading with noncritical SHG in an LN waveguide. In such waveguides spatial diffraction is suppressed, and the strong confinement implies that high-repetition rate low-energy femtosecond pump pulses can be used. LN waveguides are very mature technologically, and have been widely used for frequency conversion in integrated waveguide optics and optical communications [9], as well as for cascading [10, 11] However, they are usually fabricated by means of annealed proton exchange (APE) or titanium (Ti) in-diffusion [12, 13], which only provides a small refractive index (RI) change ($\Delta n < 0.1$) between the core and the substrate, resulting in a very limited guidance range in the mid-IR. Although the core size can be designed large to extend the cutoff wavelength, see e.g. [14], the penalty is a weak waveguide confinement leading to very high pulse energy threshold for soliton formation. The small RI change also restricts the waveguide mode to follow the material dispersion trend. Self-defocusing soliton self-compressions as well as soliton-induced supercontinuum generations (SCGs) have been investigated and demonstrated in LN waveguides with small RI change [14–17], but the pump wavelength is limited to be below the zero dispersion wavelength (ZDW), which in LN is around 2 $\mu$m.

Extending the operation range of cascaded quadratic nonlinear waveguides beyond 2 $\mu$m would be meaningful for a variety of applications such as spectroscopy and biological imaging. One way around this is to use other novel quadratic nonlinear materials that naturally support self-defocusing soliton compressions in the near- and mid-IR [18], but waveguide formation has not been studied in most of them. We therefore propose here a new LN waveguide design aiming to increase the RI change enough to substantially extend the normal dispersion regime so mid-IR self-defocusing soliton formation is possible. We achieve this by a standard ridge waveguide design, similar to our recent publication [14]. In that paper the ridge waveguide achieved confinement by being bonded to a lower-index material lithium tantalate (LT). The design allowed for extremely broadband guidance basically throughout the entire LN transmission range, and self-defocusing solitons could form without using quasi-phase matching (QPM) which the standard buried-waveguide designs in otherwise relied on [15–17]. However, since the RI change between LT and LN is small, the waveguide dispersion remained too weak to alter the material dispersion. Here we investigate a design using a substrate material with a substantially lower RI than LN. With this design an all-normal dispersion profile can be
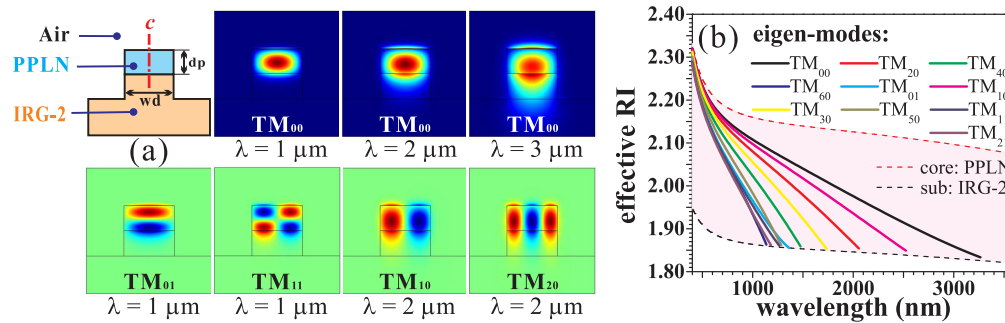
Fig. 1. (a) waveguide structure and mode field distributions of eigen-modes, at different wavelengths; (b) mode effective RIs; Waveguide has wd = 4 $\mu$m, dp = 2 $\mu$m.

achieved as a result of the strong waveguide dispersion due to the large RI change. The self-defocusing soliton dynamics with such a dispersion profile is therefore purely nonlinear. As a consequence, linear interactions such as dispersive wave (DW) generations are not occurring, which in otherwise are always accompanied with soliton formation [19], and are understood as leaky radiations from the soliton pulse. Moreover the large RI between core and substrate allows for much tighter confinement compared to previous studies, implying that sub-nano-joule (sub-nJ) femtosecond pump pulses can lead to soliton formation. This is interesting as it allows for using much lower average power femtosecond pump sources. To our knowledge such an "all-nonlinear and solitonic" waveguide or fiber device has previously never been proposed or investigated. Such a self-defocusing soliton self-compression and subsequent supercontiuum generation does, however, require imposing a moderate QPM pitch to overcome the competing self-focusing Kerr nonlinearity, in contrast to the LN/LT design in [14].

Our design relies on a material bonding technology that allows to fabricate LN waveguides with a large RI change. With surface ion implantation and wafer bonding, LN with sub-micron size scale has been proved to be bonded either to a crystal [20] or to a glass substrate [21], which actually opens the access to a variety of materials in both crystal and glass groups that can be used to fabricate a quadratic waveguide. Therefore, by choosing a substrate with much lower RI than the core, the LN waveguide can not only guide a wave in the near- and mid-IR, but also provide normal dispersion to support the self-defocusing soliton compression.

In this paper, we investigate the mode profiles and dispersion landscape of such an LN waveguide design with a large RI change. We then numerically investigate the self-defocusing soliton formation in the near- and mid-IR beyond the material ZDW, under the waveguide-induced all-normal dispersion and the cascading dominated self-defocusing nonlinearity. We also investigate a design where a small anomalous dispersion region is sandwiched between two normal dispersion regions, and show few-cycle DW formation in that region seeded by a near-IR soliton.

## 2. Waveguide structure and dispersion properties

The waveguide structure is shown in Fig. 1(a). There are varieties of candidates for the substrate material which ought to have a much lower RI than LN and good transparency in the near- and mid-IR, e.g. the potassium titanyl phosphate (KTP), the rubidium titanyl phosphate (RTP), the lithium iodate (LI), etc. in the group of crystals, or the fused silica, the fused germania, the ZBLAN, etc. in the group of glasses [22]. Here, a glass with broadband infrared transmission, specifically the Schott IRG-2 germanate glass (transparency range $0.36 \sim 4.6 \mu$m), is chosen as the waveguide substrate, see [22] for material details. The LN core layer is assumed to be
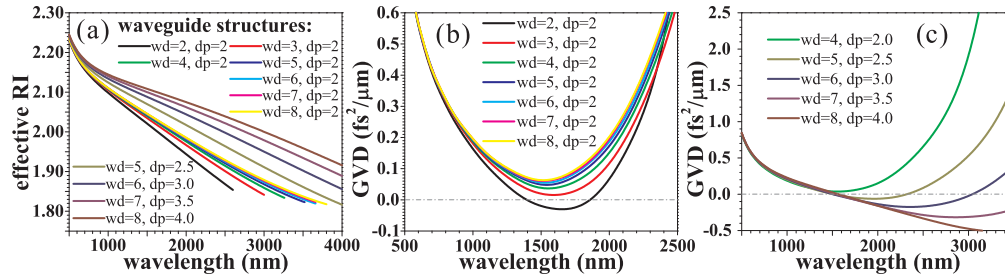
Fig. 2. dispersion tailored by tuning the core size; (a) TM$_{00}$ mode effective RI profiles and (b, c) GVD profiles with different core sizes.

bonded on the substrate and then the whole structure can be diced to have a standard ridge profile. The RI change in such a waveguide is as large as $\Delta n \approx 0.3$. Aiming at mid-IR pulse operations and making use of the strong waveguide dispersion, the waveguide size is designed to be around sub-wavelength. Eigenmodes, including both the mode propagation constants and transverse distributions, are calculated by using *Comsol Multiphiscs*. Extraordinary modes (with the polarization direction along the optic *c*-axis, marked as TM modes) at different wavelengths are shown in Fig. 1(a), while mode effective RIs are shown in Fig. 1(b). The guidance cutoff wavelength of such a waveguide can be easily extended to the mid-IR due the large RI change. Since the mode RIs are going down from the core RI to the substrate RI towards longer wavelengths, the large RI change implies a large SHG phase mismatch parameter, explaining why QPM is needed to ensure the strong cascading. Basically, waveguide dispersion always has an opposite trend to the material one, and with strong waveguide dispersion, the waveguide mode shows a typical "U"-shape GVD trend and is enabled to have normal dispersion at long wavelengths. Similar trends can also be found in step-indexed photonic crystals fibers (PCFs), which also have a large RI change [23]. Moreover, by tuning the core size (width and depth), the mode effective RI will be shifted (Fig. 2(a)) and the mode GVD profile is consequently tailored. When tuning the core width but fixing the height, the mode GVD profile is tuned mainly in the amplitude (see Fig. 2(b)) while the "U"-shape is almost preserved, with the bottom fixed at around 1.58 $\mu$m which is co-determined by the material GVD of both the core and the substrate. When enlarging the core size and keeping the aspect ratio, the GVD profile is tuned in both the amplitude and the trend (see Fig. 2(c)) as the waveguide confinement is further enhanced and the waveguide-induced normal dispersion is shifted towards longer wavelengths. It is also noticed that, to some extent, an all-normal dispersion profile can be achieved while the cutoff wavelength remains over 3 $\mu$m.

On the other hand, the transmission loss is always concerned when taking about a waveguide. Generally, the transmission loss mainly includes: 1) the insertion loss when light is coupled into and out from the waveguide (e.g. light reflection on interfaces, the mode field mismatch, etc.); 2) the material loss; and 3) the waveguide loss due to the uncertainty of the structure (e.g. the core is non-uniform along the propagation axis). Besides the material and waveguide losses, the common feeling that a small dimension waveguide is "lossy" is mainly due to the intolerable insertion loss. With a sub-wavelength structure, the waveguide eigenmodes, no matter the fundamental mode or high-order modes, turn to have strong evanescent waves and therefore the mode transverse distribution is seriously mismatched to a normal incident laser beam that has a Gaussian distribution. But the insertion loss only occurs at the frontend of the waveguide and will not impact the whole pulse propagation dynamics. In the following text, the value of the pump pulse energy or the pulse peak power that we will mention actually refers to the effective pulse energy that is launched into the waveguide, with the insertion loss already been elimi-

nated. The material loss can be ignored due to the good transparency of the material within the guidance band. Also, the waveguide loss is ignorable as the wafer bonding and the dicing technologies are supposed to give high certainty of the structure.

## 3. Nonlinear induced polarization and modal nonlinear susceptibilities

Nonlinearities in the LN waveguide include both quadratic and cubic processes, and the corresponding nonlinear induced polarizations, $\mathscr{P}_j^{(2)}$ and $\mathscr{P}_j^{(3)}$, are written as [24]:

$$\mathscr{P}_j^{(2)}(\omega) = \varepsilon_0 \sum_{\alpha_1 \alpha_2} \bar{\Theta}_{j;\alpha_1\alpha_2}^{(2)} \mathscr{F}[A_{\alpha_1} A_{\alpha_2}] \tag{1}$$

$$\mathscr{P}_j^{(3)}(\omega) = \varepsilon_0 \sum_{\alpha_1 \alpha_2 \alpha_3} \bar{\Theta}_{j;\alpha_1\alpha_2\alpha_3}^{(3)} \mathscr{F}[(1 - f_R) A_{\alpha_1} A_{\alpha_2} A_{\alpha_3} + f_R A_{\alpha_1} \mathscr{F}^{-1}[\tilde{h}_R \mathscr{F}[A_{\alpha_2} A_{\alpha_3}]]] \tag{2}$$

where j and $\alpha_{1,2,3}$ are mode marks among all TM modes. $\mathscr{F}$ indicates the Fourier transform. $A_j$ is the electric field amplitude reflecting the propagation dynamics of a waveguide mode. With the transverse distribution $B_j$, the mode electric field is defined (in frequency domain) as: $\tilde{E}(x,y,z,\omega) = \tilde{A}(z,\omega)\tilde{B}(x,y,\omega)$. $f_R$ indicates the material Raman fraction and $\tilde{h}_R$ is the Raman response spectrum. $\bar{\Theta}_{j;\alpha_1\alpha_2}^{(2)}$ and $\bar{\Theta}_{j;\alpha_1\alpha_2\alpha_3}^{(3)}$ are called ***modal nonlinear susceptibilities*** which include both the material nonlinear susceptibilities, $\bar{\chi}^{(2)}$ and $\bar{\chi}^{(3)}$, and the contributions of the mode overlap integral, $\theta_{j;\alpha_1\alpha_2}^{(2)}$ and $\theta_{j;\alpha_1\alpha_2\alpha_3}^{(3)}$ [24], i.e.: $\bar{\Theta}_{j;\alpha_1\alpha_2}^{(2)} = \bar{\chi}^{(2)} \theta_{j;\alpha_1\alpha_2}^{(2)}$, $\bar{\Theta}_{j;\alpha_1\alpha_2\alpha_3}^{(3)} = \bar{\chi}^{(3)} \theta_{j;\alpha_1\alpha_2\alpha_3}^{(3)}$, where

$$\theta_{j;\alpha_1\alpha_2}^{(2)}(\omega_1 + \omega_2) = \iint_{\text{core}} dxdy \tilde{B}_j^*(x,y,\omega_1+\omega_2) \tilde{B}_{\alpha_1}(x,y,\omega_1) \tilde{B}_{\alpha_2}(x,y,\omega_2) \tag{3}$$

$$\theta_{j;\alpha_1\alpha_2\alpha_3}^{(3)}(\sum_n \omega_n) = \iint_{\text{core}} dxdy \tilde{B}_j^*(x,y,\sum_n \omega_n) \tilde{B}_{\alpha_1}(x,y,\omega_1) \tilde{B}_{\alpha_2}(x,y,\omega_2) \tilde{B}_{\alpha_3}(x,y,\omega_3) \tag{4}$$

Mode overlap integrals $\bar{\Theta}_{j;\text{TM}_{00}\text{TM}_{00}}^{(2)}(2\omega)$ and $\bar{\Theta}_{\text{TM}_{00};\text{TM}_{00}\alpha_2\alpha_2}^{(3)}(\omega)$ are calculated in Figs. 3(a) and 3(b), which correspond to the SHG process and the Kerr self-/cross-phase modulation (SPM/XPM) effects, respectively. The material susceptibilities are $\bar{\chi}_{e;ee}^{(2)}$ ($d_{33}$) and $\bar{\chi}_{e;eee}^{(3)}$ ($c_{33}$) of the LN, since modes are extraordinary waves. It is noticed that quadratic and cubic processes within the fundamental $\text{TM}_{00}$ mode always have the highest integral value, namely the highest susceptibility, compared to processes among different modes in which the mode orthogonality leads to the decrease of the integral value. Moreover, towards longer wavelengths, the integral value is also decreased due to the reduction of the waveguide confinement.

## 4. Cascaded quadratic nonlinearity and overall self-defocusing nonlinearity

In strongly phase-mismatched SHG (between $\text{TM}_{00}$-modes of the FW and SH), cascaded quadratic nonlinearities are produced and can be quantitatively estimated as nonlinear factors [25]: $\gamma_{\text{casc},j} = \frac{\omega}{c} \tilde{n}_{2,\text{casc},j} \cdot (\theta_{j;\text{TM}_{00}\text{TM}_{00}}^{(2)})^2$, where $\tilde{n}_{2,\text{casc},j} \propto -(\bar{\chi}_{e;ee}^{(2)})^2/\Delta k_j$ is the cascaded nonlinear RI, $\Delta k_j = k_j(2\omega) - 2k_{\text{TM}_{00}}(\omega)$ is the phase mismatch parameter and $k_j$ is the mode propagation constant. The negative sign indicates a self-defocusing nonlinearity under the positive $\Delta k_j$. $\gamma_{\text{casc},\text{TM}_{00}}$ contributes most to the cascaded quadratic nonlinearity, since $\theta_{\text{TM}_{00};\text{TM}_{00}\text{TM}_{00}}^{(2)}$ is the largest among other SHGs. Analogous, SPM contributes most to the Kerr nonlinearity, which is. $\gamma_{\text{Kerr},\text{TM}_{00}} = (1 - f_R)\frac{\omega}{c} \tilde{n}_{2,\text{Kerr}} \cdot \theta_{\text{TM}_{00};\text{TM}_{00}\text{TM}_{00}\text{TM}_{00}}^{(3)}$, where $\tilde{n}_{2,\text{Kerr}} \propto \bar{\chi}_{e;eee}^{(3)}$ is the cubic nonlinear RI.
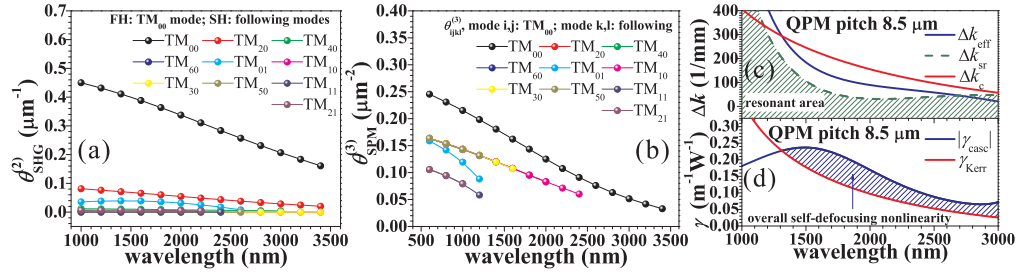
Fig. 3. (a) mode overlap integrals in SHG processes; (b) mode overlap integrals in self/cross phase modulations; (c) phase mismatch limits for overall self-defocusing nonlinearity and for clean soliton compressions; (d) nonlinear factors of both the cascaded quadratic nonlinearity and the Kerr nonlinearity. Waveguide core width is 4 $\mu$m and the height is 2 $\mu$m.

Moreover, tuning the phase mismatch by QPM, the cascaded quadratic nonlinearity can be further enhanced. The goal is to reduce the phase mismatch to increase $\tilde{n}_{2,\text{casc},j}$, but keep the effective phase mismatch $\Delta k_{\text{eff},\text{TM}_{00}} = \Delta k_{\text{TM}_{00}} - \frac{2\pi}{\Lambda}$ ($\Lambda$ is the QPM pitch size) nonzero and positive to ensure a self-defocusing cascading nonlinearity. A critical phase mismatch $\Delta k_c$ is therefore defined with which $\gamma_{\text{casc},\text{TM}_{00}} + \gamma_{\text{Kerr},\text{TM}_{00}} = 0$. $\Delta k_{\text{eff},\text{TM}_{00}}$ has to be below such a limit so that an overall self-defocusing nonlinearity can be produced. On the other hand, there also exists a lower limit, $\Delta k_{\text{sr}}$, which marks the threshold of a resonant/non-resonant cascading response [26]. The phase mismatch should stay above the threshold so that the cascading response is ultra-fast and non-resonant, and the soliton compression is clean and with high-quality.

Figure 3(c) shows both $\Delta k_c$ and $\Delta k_{\text{sr}}$. With a QPM pitch $\Lambda = 8.5$ $\mu$m, the phase mismatch is tuned to lie between the two limits. Correspondingly, $\gamma_{\text{casc},\text{TM}_{00}}$ and $\gamma_{\text{Kerr},\text{TM}_{00}}$ are shown in Fig. 3(d). An overall self-defocusing nonlinearity over a wide wavelength span $1.3 \sim 3.2$ $\mu$m is produced, with $|\gamma_{\text{casc},\text{TM}_{00}}| > \gamma_{\text{Kerr},\text{TM}_{00}}$. The phase-mismatch parameters of cascaded quadratic nonlinearities of higher-order modes, $\gamma_{\text{casc},j}$, are also tuned by QPM and may even find phase matching at short wavelengths, which will be discussed later in the paper. In the near- and mid-IR, these higher-order mode nonlinear factors are actually effectively self-focusing because the chosen QPM pitch makes their respective phase-mismatch parameters negative, but their contributions (strength) turns out to be quite weak compared to either $|\gamma_{\text{casc},\text{TM}_{00}}|$ or $\gamma_{\text{Kerr},\text{TM}_{00}}$. Therefore, within the compression window illustrated in Fig. 3(d) and recalling the normal dispersion provided in the waveguide, soliton formation in near- and mid-IR, especially beyond 2 $\mu$m, is accessible.

The dominating nonlinearity associated with soliton formation can therefore be attributed to the competition between self-defocusing cascading and self-focusing Kerr nonlinearities in the fundamental $\text{TM}_{00}$ mode, represented by the effective nonlinear parameter $\gamma_{\text{eff}} = \gamma_{\text{casc},\text{TM}_{00}} + \gamma_{\text{Kerr},\text{TM}_{00}}$. From this parameter we can calculate the effective nonlinear length as $L_{\text{N},\text{eff}} = (P\gamma_{\text{eff}})^{-1}$, where $P$ is the pulse peak power. The associated characteristic dispersion length is therefore $L_D = T_0^2 / |k_{\text{TM}_{00}}^{(2)}|$, where $T_0$ is the pulse duration and the GVD is given by $k_{\text{TM}_{00}}^{(2)} \equiv d^2 k_{\text{TM}_{00}} / d\omega^2$. Therefore, the effective soliton order is estimated as $N_{\text{eff}} = \sqrt{L_D / L_{\text{N},\text{eff}}}$.

## 5. Few-cycle self-defocusing soliton compressions beyond 2 $\mu$mum

The numerical simulations we now show use the nonlinear wave equation in frequency domain (NWEF), which is a general tool to simulate pulse propagation dynamics in a nonlinear medium. It directly deals with the pulse electric field instead of the envelope and automatically
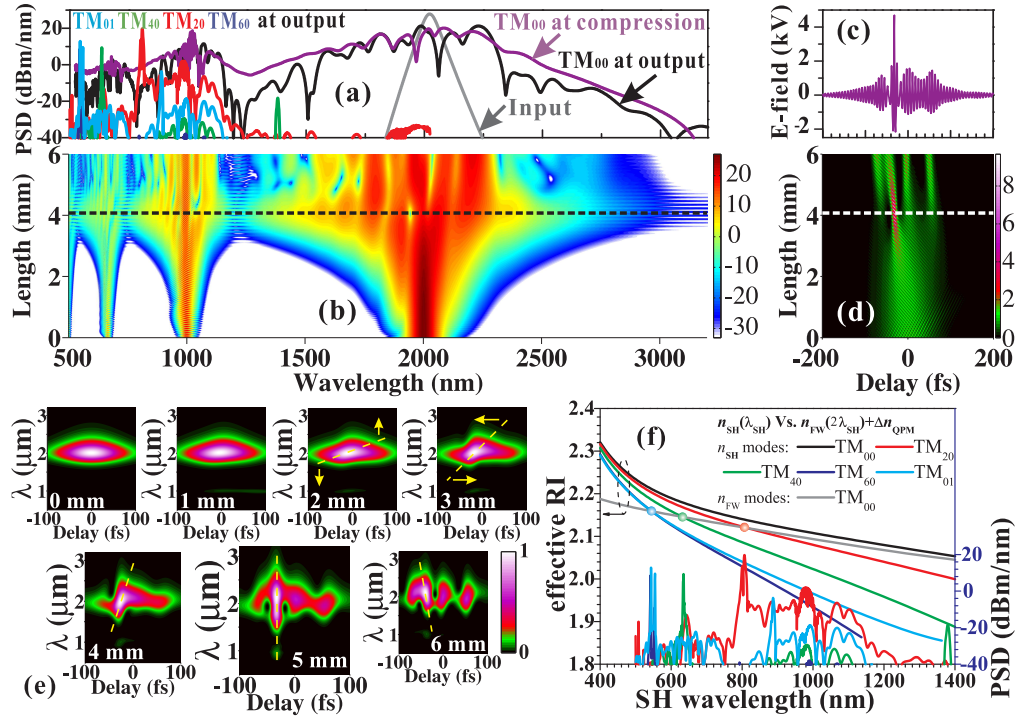
Fig. 4. numerical simulation of self-defocusing soliton compression at 2 $\mu$m in the LN waveguide; wd $= 4$ $\mu$m, dp $= 2$ $\mu$m, $\Lambda = 8.5$ $\mu$m, $\gamma_{casc,TM_{00}} = -0.169$ m$^{-1}$W$^{-1}$, $\gamma_{Kerr,TM_{00}} = 0.097$ m$^{-1}$W$^{-1}$, $k^{(2)}_{TM_{00}} = 0.151$ fs$^2/\mu$m; pump pulse has FWHM = 100 fs, energy 0.6 nJ, soliton order is $N_{eff} \approx 3$; modes taken into account are TM$_{00}$, TM$_{20}$, TM$_{40}$, TM$_{60}$ and TM$_{01}$; (a) spectra of the input pulse (TM$_{00}$ mode), the compressed pulse (TM$_{00}$ mode) and the output pulse (all modes); The spectrum is scaled in pulse spectrum density (PSD) which has the unit of dBm/nm; (b) pulse spectral evolution (TM$_{00}$ mode) with the first compression stage marked by the dash line; (c) TM$_{00}$ mode electric field amplitude at the first compression stage; (d) pulse temporal evolution (TM$_{00}$ mode); (e) pulse spectrogram evolution; (f) high-order mode SH radiations corresponding to phase matching positions.

includes all types of nonlinear interactions to the order included in the nonlinear polarization expansion [27]. In the LN waveguide with multiple modes, a group of NWEFs is used, each of them corresponds to a single mode and governs the electric field amplitude $\tilde{A}_j$, while the transverse components $\tilde{B}_j$ are degenerated through integrals [24]. The equation for each mode is written as:

$$\frac{\partial \tilde{A}_j}{\partial z} + \alpha \tilde{A}_j + ik_j(\omega)\tilde{A}_j = -i\frac{\omega^2\mu_0}{2k_j(\omega)}(\mathscr{P}^{(2)}_j(\omega) + \mathscr{P}^{(3)}_j(\omega)) \tag{5}$$

where $\alpha$ indicates the material and the waveguide losses.

First, we show the self-defocusing soliton compression at 2 $\mu$m, see Fig. 4. The waveguide has wd $= 4$ $\mu$m, dp $= 2$ $\mu$m and provides all-normal dispersion within the guiding band. The QPM pitch is chosen to $\Lambda = 8.5$ $\mu$m as to ensure a an effective defocusing nonlinearity. The pump pulse, in the TM$_{00}$ mode, has a full width at half maximum (FWHM) of 100 fs, similar to the thulium-fiber-based laser system used in [15]. The pulse peak power is 6 kW and therefore the pulse energy is around 0.6 nJ. $\alpha$ is set to zero. leading to an effective soliton order $N_{eff} \approx 3$.

Launched into the waveguide, the pulse spectrum is SPM broadened governed by the overall self-defocusing nonlinearity while a weak SH around 1 $\mu$m is accompanied due to the phase mismatched SHG process, see Figs. 4(a) and 4(b). The third harmonic and even higher order harmonics are also observed through both quadratic and cubic wave mixing processes. These harmonics look exactly like copies of the fundamental wave (FW) (in the frequency domain) but they are much weaker because they are heavily phase mismatched. Therefore they will not impact the compression of the FW. Combined with the normal dispersion, the self-defocusing phase shift can be well compensated and the pulse, in time domain, is strongly compressed through the soliton self-compression effect to almost single-cycle, see Figs. 4(c) and 4(d).

We note that LN has a strong Raman fraction ($f_R \approx 50\%$, cf. also discussion in [28]) which not only causes pulse spectral red-shift, known as soliton self-frequency shift (SSFS) effects, but also gives rise to modulation instabilities impacting both the amplitude and the phase of the pulse spectrum [29]. The latter will further cause the pulse splitting, known as the Raman fission effects, if the soliton order is larger than unity. In Fig. 4(d), the Raman fission is observed after the first compression stage (marked with the white-dashed line). The soliton pulse is also red-shifted which is not obvious from the spectral figure but clues are found from the slight change in the temporal delay Fig. 4(d), as the red-shifted spectrum will have an increased group velocity (GV) when combined with the normal dispersion. Such a slight spectral red-shifting is actually from the competition between the Raman SSFS and cascading-induced self-steepening effects which cause spectral blue-shift due to the negative GV mismatch between the FW and the SH [27].

For a deeper understanding of such a soliton compression process, the pulse spectrogram evolution, with slices at different propagation distances, is shown in Fig. 4(e). The evolution starts with the domination of the nonlinearity which stretches the pulse spectrum while maintaining the temporal shape, resulting in a tilt on the spectrogram pattern, namely inducing the nonlinear phase shift. The slope of the tilt ($\frac{d\omega}{d\tau} = C$) reflects the pulse linear chirp (factor $C$) induced by the SPM. The normal dispersion also stretches the pulse but only on the temporal shape and then the tilt of the pattern is further adjusted with the nonlinear phase shift compensated. The tilt adjustment is $\frac{d\tau}{d\omega} = -k_{\mathrm{TM}_{00}}^{(2)} \cdot z$ ($z$ is the propagation distance). The soliton compression is actually accomplished when the tilt of the pattern is turned from the initial horizonal state to the vertical state, while the compressed pulse will enter a relaxation stage upon further propagation as the tilt is overturned from the maximum compression vertical position. Typically a breather-kind of dynamics will then be observed with the soliton compressing and relaxing periodically and slowly entering into a steady state. The Raman fission is also clearly observed with mainly three fractions formed in the spectrogram pattern.

Moreover, while most energy remains in the $\mathrm{TM}_{00}$ mode, sharp-peak radiations are observed in high-order modes (Fig. 4(a)), which exactly correspond to the phase matching SHGs with SHs among high-order modes, see Fig. 4(f). The phase-matching condition scaled in RI is:

$$n_{\mathrm{SH,j}}(\lambda_{\mathrm{SH}}) = n_{\mathrm{FW,TM}_{00}}(2\lambda_{\mathrm{SH}}) + \Delta n_{\mathrm{QPM}}(\lambda_{\mathrm{SH}}) \tag{6}$$

where $\Delta n_{\mathrm{QPM}} = \frac{\lambda_{\mathrm{SH}}}{\Lambda}$ and $\lambda_{\mathrm{SH}}$ is the SH wavelength. However, due to their small modal nonlinear susceptibilities these radiations are weak in a similar way as the higher harmonics within the $\mathrm{TM}_{00}$ mode described above, and they will therefore not impact the soliton compression process either.

The scenario of self-defocusing soliton compression also works at other wavelengths, e.g. at 1.41 $\mu$m shown in Fig. 5, at 1.58 $\mu$m shown in Fig. 6 and at 3 $\mu$m shown in Fig. 7, in which the soliton pulse can always be compressed to few-cycle and even single cycle. The waveguide for the 3 $\mu$m compression has a bigger size, wd = 5 $\mu$m, dp = 2.5 $\mu$m and the cutoff wavelength is extended to over 4 $\mu$m. From these simulations we conclude that when
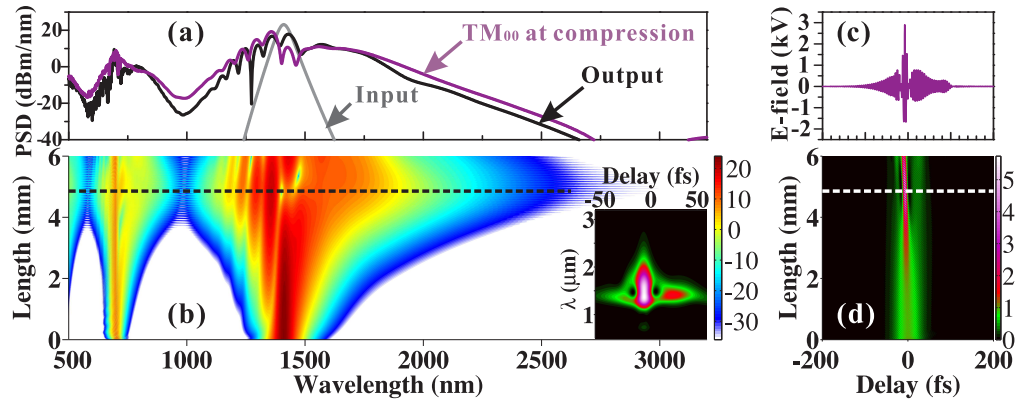
Fig. 5. numerical simulation of self-defocusing soliton compression at 1.41 $\mu$m in the LN waveguide; waveguide has the same structure as Fig. 4; pump pulse has FWHM = 50 fs, energy 0.2 nJ, soliton order is $N_{eff} \approx 1.5$; (a) TM$_{00}$ mode spectra of the input pulse, the compressed pulse and the output pulse; (b) pulse spectral evolution (TM$_{00}$ mode) with the first compression stage marked by the dash line; (c) TM$_{00}$ mode electric field amplitude at the first compression stage; (d) pulse temporal evolution; insert: pulse spectrogram at the first compression stage.
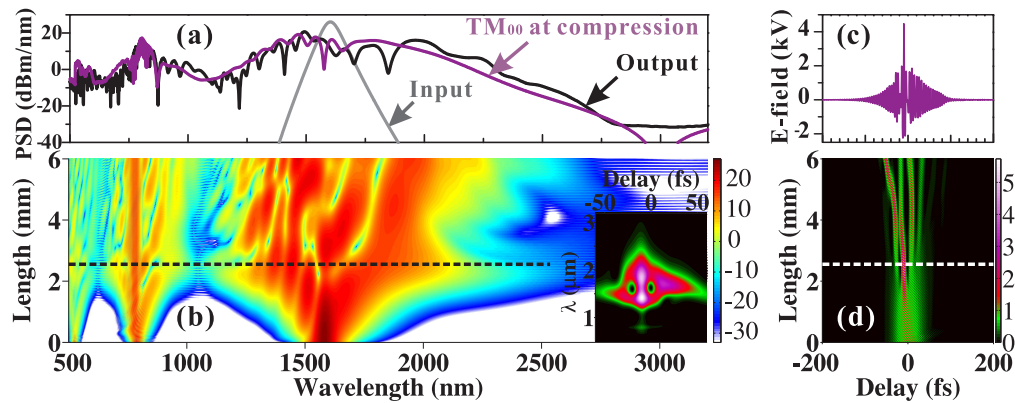


Fig. 6. numerical simulation of self-defocusing soliton compression at 1.58 $\mu$m in the LN waveguide; waveguide has the same structure as Fig. 4; pump pulse has FWHM = 50 fs, energy 0.5 nJ, soliton order is $N_{eff} \approx 4$; (a) TM$_{00}$ mode spectra of the input pulse, the compressed pulse and the output pulse; (b) pulse spectral evolution (TM$_{00}$ mode) with the first compression stage marked by the dash line; (c) TM$_{00}$ mode electric field amplitude at the first compression stage; (d) pulse temporal evolution; insert: pulse spectrogram at the first compression stage.

having a small soliton order $1 < N_{eff} < 2$, the compressed soliton has a quite clean temporal shape as well as a clean pulse spectrogram pattern, due to the suppression of Raman fission effects. When the soliton order $N_{eff} > 2$, the compressed pulse will have a complex figure in both the pulse shape and the spectrogram pattern. The few-cycle soliton compression also leads to supercontinuum generation, which can easily span over an octave in the spectrum in the near- and mid-IR (at the -20 dB level). Although the pump pulse has a sub-nJ energy, the pulse spectrum density is still high, which is a consequence of the strong confinement provided by this waveguide design.
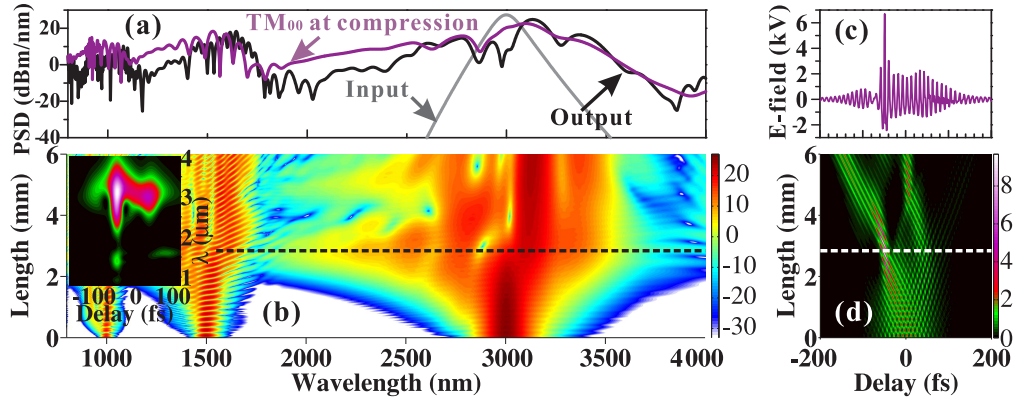
Fig. 7. numerical simulation of self-defocusing soliton compression at 3 $\mu$m in the LN waveguide; wd = 5 $\mu$m, dp = 2.5 $\mu$m, $\Lambda = 10$ $\mu$m, $\gamma_{\text{casc,TM}_{00}} = -0.063$ m$^{-1}$W$^{-1}$, $\gamma_{\text{Kerr,TM}_{00}} = 0.030$ m$^{-1}$W$^{-1}$, $k^{(2)}_{\text{TM}_{00}} = 0.531$ fs$^2$/$\mu$m; pump pulse has FWHM = 100 fs, energy 1.2 nJ, soliton order is $N_{\text{eff}} \approx 1.5$; (a) TM$_{00}$ mode spectra of the input pulse, the compressed pulse and the output pulse; (b) pulse spectral evolution (TM$_{00}$ mode) with the first compression stage marked by the dash line; (c) TM$_{00}$ mode electric field amplitude at the first compression stage; (d) pulse temporal evolution (TM$_{00}$ mode); insert: pulse spectrogram at the first compression stage.

If there are material and waveguide losses (additional to the insertion loss), e.g. $\alpha = 0.69$/cm for -3 dB/cm loss, soliton compressions as well as SCGs will be impacted. Since the soliton order is gradually decreased during the propagation, the anticipated pulse spectral broadening will shrink, which implies a degraded soliton compression.

Let us now investigate the spectral coherence of these soliton pulses. The pump pulse is assumed to contain a *one-photon-per-mode* (OPPM) noise figure ($\frac{h\omega}{\Delta\omega}e^{i\phi_{\text{rand}}}$, where $h$ is the Planck constant, $\omega$ is the frequency, $\Delta\omega$ is the frequency resolution of the simulation window and $\phi_{\text{rand}}$ is a random phase between $0 \sim 2\pi$) [30].

The first order spectral coherence $\tilde{g}^{(1)}_{12}$ is then calculated from several simulation shots, i.e.:

$$\tilde{g}^{(1)}_{12}(\omega) = \frac{\left|\left\langle \tilde{A}^*_s(\omega)\tilde{A}_l(\omega)\right\rangle\right|}{\sqrt{\left\langle \left|\tilde{A}_s(\omega)\right|^2\right\rangle \left\langle \left|\tilde{A}_l(\omega)\right|^2\right\rangle}}, \; s \neq l \qquad (7)$$

where $s$ and $l$ marks the simulation shot. The angle brackets indicate averaging over noise realizations.

The coherence of the output pulse spectrum in both the 2-$\mu$m and 3-$\mu$m compressions are shown in Fig. 8. The pulse spectrum in the near- and mid-IR is demonstrated to be highly coherent and the $\tilde{g}^{(1)}_{12}$ value is almost unity since the noise figure at lower frequency is weaker, while for shorter wavelengths where harmonics are generated, the coherence of the pulse spectrum is slightly reduced.

Such a high coherence is physically attributed to the low soliton order of the femtosecond pump that the noise-sensitive soliton fission regime and the pulse modulation instability (MI) are suppressed, compared to typical SCGs in PCFs which usually use picosecond pumps around the ZDW, with the soliton order over 100, so that strong soliton fission and MI is induced and the spectral coherence will be decreased [30]. Similar spectral high coherence is also observed in an all-nonlinear but non-solitary SCG process in [23] which is operated in the PCF designed
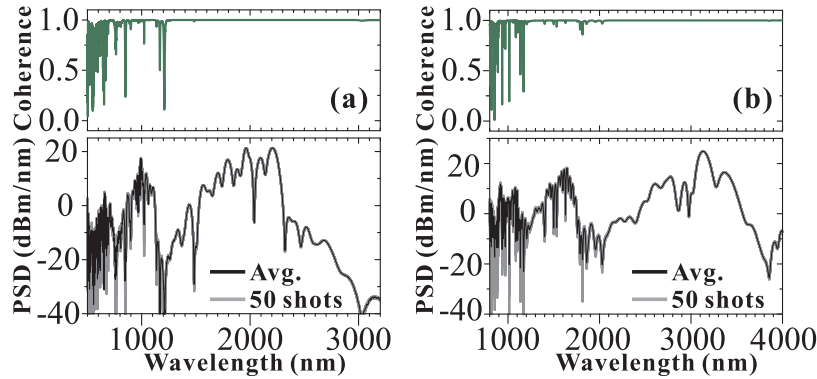
Fig. 8. coherence spectra for the output pulse spectrum in both the (a) 2-$\mu$m and (b) 3-$\mu$m compressions.

to have all-normal dispersion and is dominated by the SPM from the traditional self-focusing Kerr nonlinearity.

## 6. DW generation and soliton spectral tunneling

It is well-known that a soliton will radiate DWs when the dispersive phase (spectral propagation constant profile) is perturbed with high-order dispersion (third-order dispersion, fourth-order dispersion, etc.). In the present case that the soliton exists in the normal dispersion regime, the necessary condition for the DW generation is "the presence of an anomalous dispersion region". More precisely, according to the DW phase matching condition, DWs are predicted to be generated exactly in the anomalous dispersion region(s) if the major perturbation comes from the third-order dispersion. However, if presence of fourth-order dispersion, DWs can be generated either in anomalous or normal dispersion regions. The latter is actually revealed to be the soliton spectral tunneling (SST) effect in which the DW can actually form another soliton state, and an opposite dispersion region is considered as a necessary barrier [31].

Therefore, with an all-normal dispersion profile in the LN waveguide, DWs are suppressed for sure, see Fig. 5 and Fig. 6. The waveguide for the 3 $\mu$m compression actually has two ZDWs (1.51 $\mu$m and 2.30 $\mu$m), indicating an anomalous dispersion region sandwiched by two normal dispersion regions. However, DWs are still suppressed since the pumping wavelength is far away from the ZDWs and the DW phase-matching condition is not satisfied. Thus, without such linear radiations, the soliton dynamics is purely nonlinear.

On the other hand, when pumping close to one of the two ZDWs, DW generations are expected. Moreover, with the soliton spectral shifting and compression/relaxation breathing, the DW radiations can also form a few-cycle pulse [32].

We show a 2.2-$\mu$m pulse generation by means of such a breathing DW generation, see Fig. 9. The waveguide again has wd = 5 $\mu$m and dp = 2.5 $\mu$m. The QPM pitch is chosen to $\Lambda = 9.8$ $\mu$m to give an effective defocusing nonlinearity. The pump wavelength is chosen to 1.35 $\mu$m, which has phase matching to a DW at around 2.2 $\mu$m. The pump pulse has a FWHM of 25 fs so that an ultra-broadband spectrum is provided with large sideband energy at the DW position. The pulse energy is 0.1 nJ and the soliton order is $N_{\text{eff}} \approx 1$. The pulse spectrogram evolution is also investigated to help understanding the whole process, see Fig. 9(a) When launched into the waveguide, the soliton at 1.35 $\mu$m starts to transfer energy to the DW, and the soliton itself is spectrally blue shifted mainly due to a recoil effect [33, 34] (The cascading-induced blue shift and the Raman SSFS are almost balanced with each other). The soliton blue shift
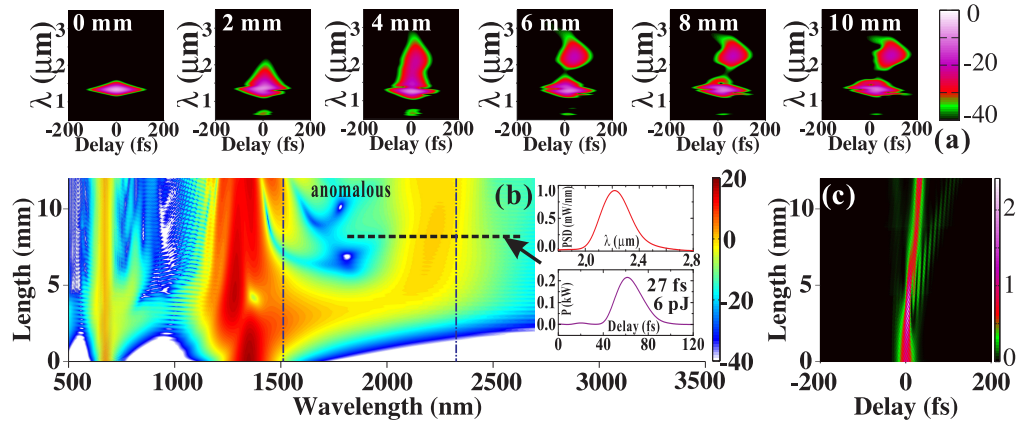
Fig. 9. broadband DW generation at 2.2 $\mu$m in the LN waveguide when pumping at 1.35 $\mu$m; wd = 5 $\mu$m, dp = 2.5 $\mu$m, $\Lambda = 9.8$ $\mu$m, $\gamma_{\mathrm{casc,TM_{00}}} = -0.217$ m$^{-1}$W$^{-1}$, $\gamma_{\mathrm{Kerr,TM_{00}}} = 0.152$ m$^{-1}$W$^{-1}$, $k^{(2)}_{\mathrm{TM_{00}}} = 0.049$ fs$^2$/$\mu$m; pump pulse has FWHM = 25 fs, energy 0.1 nJ, soliton order is $N_{\mathrm{eff}} \approx 1$; (a) pulse spectrogram evolution with slices at different propagation distance; (b) spectral evolution (TM$_{00}$ mode); dash-dot lines mark the two ZDWs; (d) temporal evolution (TM$_{00}$ mode); insert: DW pulse spectrum and temporal shape.

is reflected by the temporal delay shown in Fig. 9(c). Meanwhile, the soliton is further compressed and more energy is transferred out to the DW, with a red-shifted DW position due to the phase-matching condition to the blue shifted soliton, see Fig. 9(b). However, with energy continuously transferred out, the soliton is weakened with the soliton order going below the unity. Then, the soliton will self-adapt to maintain a soliton state by narrowing its pulse spectrum and broadening the temporal shape. A breath is therefore established, with the compression-induced spectral broadening and self-adaptive spectral narrowing, leaving a clean "DW pulse" pattern at 2.2 $\mu$m in the spectrogram. By applying a long-pass filter the DW-part of the spectrum is then filtered out so it can be analyzed in detail. It spans $2.0 \sim 2.6$ $\mu$m (at -10 dB level) and the pulse duration is estimated to be around 3.5-optical cycles (FWHM = 27 fs), see the insert in Fig. 9. The conversion efficiency is 6% leading to a pulse energy of 6 pJ.

It is noted that such a DW pulse is actually located in the anomalous GVD region and therefore it could not form a soliton. However, since the GVD in this regime is very weak, the temporal pulse shape will be almost unaffected even over a long propagation distance while spectral phase is accumulated by the self-defocusing nonlinearity.

The SST effect is also investigated in the same waveguide, with a more precise designing on the phase matching. The pump wavelength is set to be at 1.31 $\mu$m and the DW is therefore to be generated at 2.6 $\mu$m where the dispersion is also normal; thus, the DW can form a soliton state. We here keep the name "dispersive wave", as the phase-matching condition is found by intersecting the near-IR "parent" soliton dispersion curve, which is inherently dispersionless, with a dispersion curve that reflects the mode dispersion. Whether the formed DW is then energetic enough to form a soliton state that does not disperse, and thereby will not be a dispersive wave per se any more, is another matter. Moreover, both the parent soliton and the DW also have the same GV, as the GV-matching condition is satisfied, under which the energy transferred from the parent soliton to the DW will also be transferred back, reflecting a so-called soliton coupling effect [35]. Figure 10(a) shows how the soliton coupling evolves. Both the parent soliton and the DW spectra are periodically changed during the evolution, with the energy coupling in
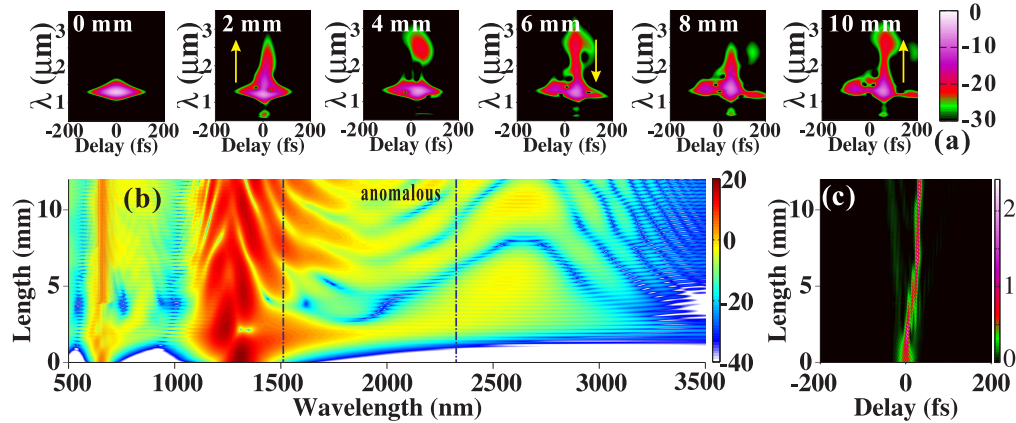
Fig. 10. soliton spectral tunneling effect with the pump at 1.31 $\mu$m and the DW pulse generated at 2.6 $\mu$m which is also solitonary; wd = 5 $\mu$m, dp = 2.5 $\mu$m, $\Lambda = 9.8$ $\mu$m, $\gamma_{\text{casc,TM}_{00}} = -0.204$ m$^{-1}$W$^{-1}$, $\gamma_{\text{Kerr,TM}_{00}} = 0.159$ m$^{-1}$W$^{-1}$, $k^{(2)}_{\text{TM}_{00}} = 0.063$ fs$^2/\mu$m; pump pulse has FWHM = 25 fs, energy 0.175 nJ, soliton order is $N_{\text{eff}} \approx 1$; (a) pulse spectrogram evolution with slices at different propagation distance; dash-dot lines mark the two ZDWs; (b) spectral evolution (TM$_{00}$ mode); (d) temporal evolution (TM$_{00}$ mode).

between (Fig. 10(b)). When having two solitons in the spectrogram, the temporal shape shows a interferometric signal (Fig. 10(c)).

Compared to the SST effect, the 2.2-$\mu$m DW pulse generated in Fig. 9 cannot couple back to the near-IR soliton exactly because it is not GV-matched to the parent soliton, and it will therefore travel away from the parent soliton (this is quite unique to self-defocusing DW generations, see also the discussion in [36]). Through SST, the parent soliton energy may be fully coupled to the DW pulse, provided that a spectral red-shift occurs, such as Raman SSFS [31]. However, with the cascading process, Raman SSFS is in most cases counterbalanced by cascading induced self-steepening effects, and the spectrum shows blue-shift dominated by the recoil effect, which unfortunately reduces the coupling efficiency. On the other hand, both cases are demonstrated to have also a high spectral coherence.

## 7. Conclusion

As a conclusion, in this paper we proposed an LN waveguide design with a large refractive index (RI) change, a design intended to extend self-defocusing soliton formation further into the mid-IR. The large RI change is suggested to come from bonding an LN wafer containing a ridge waveguide on top of a glass substrate with broadband IR transmission and substantially lower RI than LN, here chosen to be the Schott glass IRG-2. Self-defocusing solitons require normal dispersion and an effective self-defocusing nonlinearity, here originating from cascaded SHG, to form. Compared to bulk LN or traditional low-RI LN waveguide designs, in which the dispersion trend limits the compression to be below the zero-dispersion wavelength (ZDW) at around 2 $\mu$m, the proposed design significantly extends the soliton regime of LN waveguides into the mid-IR. This occurs due to the strong waveguide dispersion that can significantly alter and even counterbalance the material dispersion. Thus, the normal dispersion regime can be extended well beyond the material ZDW. It is even possible to create an all-normal dispersion profile (within the waveguide cutoff frequencies) by properly tuning the waveguide core size. Such an all-nonlinear and solionic waveguide or fiber design has to our knowledge not been investigated before. The large RI change also has the benefit of supporting broadband guidance

well into the mid-IR, and at the same time keep the waveguide core size small (in contrast to a broadband low-RI design [14]). The large confinement from the small core leads to a very low-energy soliton threshold, implying that the pump source can operate at much lower average powers or higher repetition rates than traditional LN waveguide designs. Moreover, an effective self-defocusing nonlinearity can be found over a broadband range in near and mid-IR, where the cascaded SHG self-defocusing nonlinearity counterbalances the material Kerr nonlinearity. In order to achieve this a moderate QPM pitch on the order of 10 $\mu$m has to be used.

Formation and dynamics of self-defocusing solitons at 2 $\mu$m, 3 $\mu$m and other wavelengths were numerically investigated, in which single-cycle pulses can be generated through the soliton self-compression effect, followed by octave-spanning supercontinuum generation in sub-cm length waveguides. Using a 100 fs pump pulse and keeping a low soliton order, the pulse spectrum was demonstrated to be highly coherent. We attribute this to the purely nonlinear soliton dynamics and the suppression of the soliton fission and the modulation instability. For designs where the dispersion profile does have ZDWs, an anomalous-dispersion region could be found sandwiched between two normal-dispersion regimes. In this scenario DW generation as well as the soliton self-tunneling (SST) effect were investigated. The DWs could manifest as few-cycle pulses under a breathing regime induced by the spectral soliton shift and compression/relaxation processes of the parent soliton. With the SST effect, a group-velocity matching condition enables the energy coupling between the DW and the parent soliton, and in this case the wavelength of the DW phase-matching point pulse is actually located in the long-wavelength normal dispersion region beyond the anomalous dispersion regime, and therefore may form a soliton state.

Executing the proposed design should not pose too many obstacles, and it therefore has a number of exciting advantages over traditional designs, both from a nonlinear science viewpoint and from an application viewpoint. Such waveguides could lead to more effective ways of generating few-cycle pulses and highly coherent supercontinua with low-energy femtosecond pulses in near and mid-IR.

### Acknowledgments